INORGANIC CHEMISTRY FRONTIERS

RESEARCH ARTICLE

View Article Online
View Journal | View Issue

Cite this: *Inorg. Chem. Front.*, 2024, **11**, 7843

Shooting short-wavelength nonlinear optical materials with targeted balance performances in hydroxyborates through first-principles high-throughput screening†

Chenxu Li,‡[a,b,c] Abudukadi Tudi, ‡[a,b] Huanhuan Cheng,[a,b] Qingyu Liu,[a,b] Zhihua Yang *[a,b] and Shilie Pan *[a,b]

Received 3rd September 2024,
Accepted 4th October 2024

DOI: 10.1039/d4qi02234c

rsc.li/frontiers-inorganic

Aiming to discover short-wavelength ultraviolet (UV) excellent nonlinear optical (NLO) materials, we used the first-principles high-throughput screening pipeline for hydroxyborate NLO materials. We systematically assessed over 222 non-centrosymmetric (NCS) compounds from 718 hydroxyborates in the Inorganic Crystal Structure Database (ICSD), employing screening criteria based on band gaps, the shortest phase-matching (PM) wavelengths, and second harmonic generation (SHG) coefficients. Three crystals are identified as promising short-wavelength UV NLO materials, with their PM SHG capacity extending to the solar blind region (200–280 nm). Additionally, an investigation on the relationship among the birefringence, the dimensionality of the B–O/OH anionic framework, and the (A + OH)/B (where A represents metal cations) ratio was conducted on screened hydroxyborates to illuminate the exploration of hydroxyborates with desirable short PM wavelengths for NLO properties.

Introduction

Nonlinear optical (NLO) materials for second harmonic generation (SHG) experienced rapid development after the pioneering experiment employing quartz crystals in 1961.[1] Second-order NLO crystals are extensively utilized in scientific and industrial fields, including applications in free-space communication, spectroscopy, industrial processing, medical diagnosis, and environmental monitoring.[2–5] NLO crystals are categorized into three major groups based on their operational wavelength ranges: short-wavelength (ultraviolet, UV, 100 ≤ λ ≤ 400 nm: long-wave ultraviolet, UVA: 320–400 nm; medium-wave ultraviolet, UVB: 280–320 nm; solar blind, UVC: 200–280 nm; and deep-ultraviolet, UVD: 100–200 nm), visible/near-infrared (vis–NIR, 0.4–3 μm), and middle/far-infrared (M-F-IR, including the atmospheric transparent windows of 3–5 and 8–13 μm). Particularly, with the swift progress in short-wavelength all-solid-state laser technology, short-wavelength NLO crystals have emerged as a focal point of research.[6–20] Various types of NLO crystals have been discovered, encompassing borates, silicates, phosphates, carbonates, nitrates, sulfates, *etc.*[21–32] Borate systems are preferred for investigating short-wavelength NLO crystals due to their abundant structural chemistry and excellent properties. Available borate NLO crystals, such as $KBe_2BO_3F_2$ (KBBF),[33] β-BaB_2O_4 (BBO),[34] LiB_3O_5 (LBO),[35] and $CsLiB_6O_{10}$ (CLBO),[36] are utilized to fulfill the application demands of the short-wavelength region due to their advantageous properties, including broad transparency ranges, short phase-matching (PM) ability (sufficient birefringence), and so on.

Hydroxyborate crystals, as a class of crystal materials, have demonstrated immense potential in the field of nonlinear optics in recent years. The oxygen atom of [BO_3] and [BO_4] bonds with hydrogen atoms to create [$BO_x(OH)_{3-x}$] (x = 0–2) and [$BO_y(OH)_{4-y}$] (y = 0–3) units. The incorporation of hydrogen atoms eliminates the dangling bonds of terminal oxygen, thereby enhancing the energy gap. Additionally, hydrogen bonds may serve to optimize the arrangement of anionic units.[37] Nevertheless, there is a lack of exploration as to whether hydroxyborates are potential short-wavelength NLO materials owing to the complexity of microstructures.

With the advancement of high-performance computing resources and the enhanced precision of first-principles

[a]*Research Center for Crystal Materials, State Key Laboratory of Functional Materials and Devices for Special Environmental Conditions, Xinjiang Key Laboratory of Functional Crystal Materials, Xinjiang Technical Institute of Physics and Chemistry, Chinese Academy of Sciences, 40-1 South Beijing Road, Urumqi 830011, China. E-mail: zhyang@ms.xjb.ac.cn, slpan@ms.xjb.ac.cn*
[b]*Center of Materials Science and Optoelectronics Engineering, University of Chinese Academy of Sciences, Beijing 100049, China*
[c]*School of Medical Engineering and Technology, Xinjiang Medical University, Urumqi 830000, China*

†Electronic supplementary information (ESI) available. See DOI: https://doi.org/10.1039/d4qi02234c

‡These authors contributed equally to this work.

methods, the prediction and screening of new functional materials through the first-principles approach are becoming potent methods for accelerating materials development. High-throughput screening technology, based on density functional theory (DFT), is well-regarded for its efficiency and accuracy across diverse domains such as photovoltaic applications[38,39] and superconductivity.[40,41] This approach presents a promising solution to the challenge. Leveraging the development of massive materials databases like the Materials Project[42] and the Inorganic Crystal Structure Database (ICSD),[43] high-throughput screening facilitates the rapid and precise evaluation of vast compound libraries, thereby significantly augmenting research efficiency.

In this work, we devised a high-throughput computational strategy to identify excellent short-wavelength NLO materials. Initially, we screened 222 non-centrosymmetric (NCS) compounds from 718 hydroxyborates in the ICSD and then a total number of 60 candidates were identified for further analysis. The compounds with balanced short-wavelength NLO properties of large E_g > 3.1 eV (λ_{cutoff} < 400 nm), strong SHG efficiency (>0.39 pm V^{-1}), and the shortest PM wavelengths λ_{PM} < 400 nm were screened out.

Through a meticulous screening process involving structural optimization, property simulation, and mechanism analysis, we identified several promising SHG materials. With the operational wavelength in the solar blind (UVC) region (200–280 nm), $KCa_4(B_{22}O_{32}(OH)_{10}Cl)\cdot 4H_2O$, $Ca_2(B_5O_8(OH))_2B(OH)_3\cdot H_2O$, and $NH_4(B_5O_6(OH)_4)\cdot 2H_2O$ have shown potential. With the operational wavelength in the medium-wave ultraviolet (UVB) region (280–320 nm), $Na_4(B_{10}O_{16}(OH)_2)\cdot 4H_2O$ and $Ba_2(B_6O_9(OH)_4)$ have been identified as suitable candidates. Furthermore, with the operational wavelength in the long-wave ultraviolet (UVA) region (320–400 nm), $Ca_9B_{26}O_{34}(OH)_{24}Cl_4\cdot 13H_2O$, $Na_2Ba_2(B_{10}O_{17}(OH)_2)$, $(Na(H_2O))_2(B_5O_8(OH))$, and $CaB_3O_5(OH)$ have been recognized as potential materials. Furthermore, to clarify the origin of the difference in birefringence, we analyzed the influence of the B–O/OH anionic framework, the arrangement and the density of anionic groups, particularly the π-conjugated [BO_3], [$B(OH)_3$], and [$BO_2(OH)$] units. Our results suggest that hydroxyborates possess the potential to manifest short PM wavelengths for NLO properties. This study contributes to the advancement and exploration of promising short-wavelength NLO materials within the hydroxyborate system.

Computational methods

In this work, the hydroxyborate crystals were collected in the ICSD (Version 5.1.0 build 20231115-1151) by high-throughput screening methodology. We can obtain target compounds by searching structures that include B, O, and H elements.

To further screen the target NLO materials, the first-principles calculations of the optoelectronic properties of selected crystals were used by employing the DFT method in the CASTEP package.[44,45] The generalized gradient approximation (GGA)[46] within the Perdew–Burke–Ernzerhof (PBE)[47] functional and the norm-conserving pseudopotential[48] was adopted to describe the exchange–correlation energy, with a high plane-wave energy cutoff of 750 eV. The Monkhorst–Pack *k*-point separation for each compound was set as 0.04 1/Å in the Brillouin zone for SCF and 0.04 1/Å for optics calculation, resulting in the corresponding Monkhorst–Pack *k*-point meshes for the structure relaxation and property calculations. The self-consistent field (SCF) calculations were performed with a convergence criterion of 1×10^{-6} eV per atom on the total energy. The empty bands were set as 3 times that of valence bands in the calculation to ensure the convergence of optical properties. Other calculation parameters and convergent criteria were set as the default values of the CASTEP package.

In addition, the Heyd–Scuseria–Ernzerhof (HSE06) hybrid functional[49–51] was adopted for more accurate band gaps. The band gap differences between the GGA-PBE and HSE06 methods were used as scissor operators for more accurate calculations of birefringence and SHG coefficients. The HSE06 hybrid density functional theory was executed using the plane-wave code (PWmat). The NCPP-SG15-PBE pseudopotential and 50 Ryd plane wave cutoff energy were used in the calculation,[52,53]

$$E_{XC}^{HSE} = \alpha E_X^{HF,SR}(\mu) + (1-\alpha)E_X^{PBE,SR}(\mu) + E_X^{PBE,LR}(\mu) + E_C^{PBE} \quad (1)$$

where α is the mixing parameter and μ is an adjustable parameter controlling the short range of the interaction. The standard value of α is 0.25, $E_X^{HF,SR}$ and $E_X^{PBE,LR}$ are the short-term and long-term components of the PBE exchange functional, and E_C^{PBE} is the PBE correlation energy.[54]

At zero frequency, the formula of static second-order NLO coefficients can be described as[55–58]

$$\chi^{\alpha\beta\gamma} = \chi^{\alpha\beta\gamma}(\mathrm{VH}) + \chi^{\alpha\beta\gamma}(\mathrm{VE}) \quad (2)$$

where the virtual hole (VH) process $\chi^{\alpha\beta\gamma}$(VH) and virtual electron (VE) process $\chi^{\alpha\beta\gamma}$(VE) are calculated using the following formulae:

$$\chi^{\alpha\beta\gamma}(\mathrm{VH}) = \frac{e^3}{2\hbar^2 m^3}\sum_{vv'c}\int\frac{d^3k}{4\pi^3}P(\alpha\beta\gamma)\mathrm{Im}[p^{\alpha}_{vv'}p^{\beta}_{v'c}p^{\gamma}_{cv}] \times\left(\frac{1}{\omega_{cv}{}^3\omega_{v'c}{}^2}+\frac{2}{\omega_{vc}{}^4\omega_{cv'}}\right) \quad (3)$$

$$\chi^{\alpha\beta\gamma}(\mathrm{VE}) = \frac{e^3}{2\hbar^2 m^3}\sum_{vcc'}\int\frac{d^3k}{4\pi^3}P(\alpha\beta\gamma)\mathrm{Im}[p^{\alpha}_{vc}p^{\beta}_{cc'}p^{\gamma}_{c'v}] \times\left(\frac{1}{\omega_{cv}{}^3\omega_{vc'}{}^2}+\frac{2}{\omega_{vc}{}^4\omega_{c'v}}\right) \quad (4)$$

Here, α, β, and γ are Cartesian components, v and v′ denote valence bands, and c and c′ denote conduction bands. $P(\alpha\beta\gamma)$ indicates full permutation and explicitly shows the Kleinman symmetry of the NLO coefficients. The band energy difference

and momentum matrix elements are denoted as $\hbar\omega_{ij}$ and p_{ij}^{α}, respectively, and they are all implicitly k-dependent.

Results and discussion

High-throughput screening framework

To ensure the objectivity and impartiality of our screening results, we systematically screened 2075 inorganic compounds including B, O, and H elements from the ICSD. By analyzing the structures, we can determine the positional relationship between boron atoms and hydroxyl groups, identifying a total of 718 hydroxyborate compounds, of which 222 compounds show non-centrosymmetry. These 222 compounds are categorized according to their crystal systems, as shown in Fig. 1. The 222 compounds crystallize in triclinic (14 compounds, accounting for 6.3%), monoclinic (78, 35.1%), orthorhombic (52, 23.4%), trigonal (57, 25.7%), tetragonal (10, 4.5%), hexagonal (9, 4.0%), and cubic (2, 0.9%) crystal systems, respectively. Detailed information about these candidates is provided in Table S1.† During the screening process, cations which are free of d–d, f–f, or f–d electronic transitions are preferred since they could facilitate transparency attaining short-wavelength spectral ranges. Generally, these cations include alkali and alkaline-earth metal cations, some main group metal cations, and transition metal cations with a d10 electronic structure. Among the obtained structures, some of them will be excluded, including compounds with position-disorder, organic–inorganic hybrids, solid solutions, and unlocated H atoms compounds. Finally, 60 crystal structures are successfully screened out, abbreviated as $A_xB_mO_n(OH)_y$ (involving A (metal cations), B, O, and H elements).

Considering the shearing effect of metal cations and hydroxyl group, the (A + OH)/B ratio, denoted as $(x + y)/m$, represents the anionic structures and their dimensions of the compounds mentioned, as illustrated in Fig. 2 and 3. Based on the classification according to the dimensions of the anionic framework within hydroxyborates available, the percentages increase in the following order: 3D frameworks (8.33%, Table S5 in the ESI†), 1D infinite chains (11.67%, Table S3 in the ESI†), 0D isolated clusters (31.67%, Table S2 in the ESI†), and 2D infinite layers (48.33%, Table S4 in the ESI†). The (A + OH)/B ratio ranges from 1 to 3.5, 0.6 to 1.33, 0.5 to 1, and 0.67 to 1.27 among 0D, 1D, 2D, and 3D hydroxyborates, respectively. Generally, as the (A + OH)/B ratio decreases, the dimensions of the B–O/OH anionic framework increase. The intervals of (A + OH)/B ratios from 0D to 3D B–O/OH anionic structures exhibit an overlap. For instance, $K(B_5O_6(OH)_4)\cdot 2H_2O$, $RbB_5O_6(OH)_4\cdot 2H_2O$, and $(NH_4)(B_5O_6(OH)_4)\cdot 2H_2O$ with 0D $[B_5O_6(OH)_4]$ isolated clusters, $Ba_2(B_4O_7(OH)_2)$ with 1D $^1[B_4O_7(OH)_2]_\infty$ infinite chains, and $Li_2CsB_7O_{10}(OH)_4$ with 2D $^2[B_7O_{10}(OH)_4]_\infty$ infinite layers as well as $Li_3(B_5O_8(OH)_2)$ with 3D $^3[B_5O_8(OH)_2]_\infty$ frameworks all show an (A + OH)/B ratio of 1. The correlation between the various dimensions of B–O/OH anionic frameworks and the (A + OH)/B ratio suggests that the dimensionality of B–O/OH anionic frameworks can be controlled by adjusting the molar ratios of metal cations, hydroxyl group, and boron atoms.

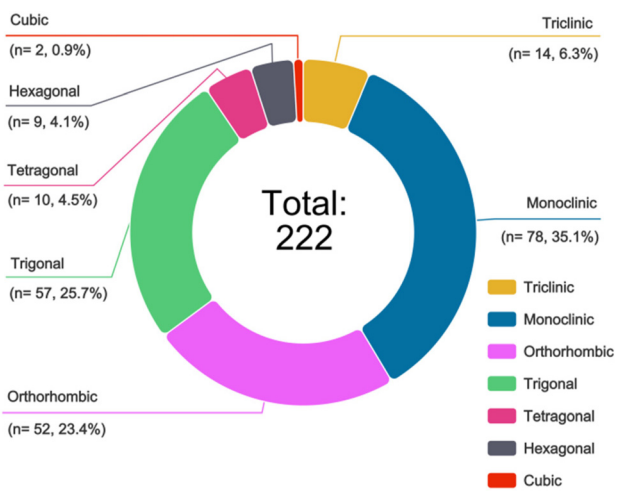

Fig. 1 Crystal system distribution of 222 NCS hydroxyborate crystals.

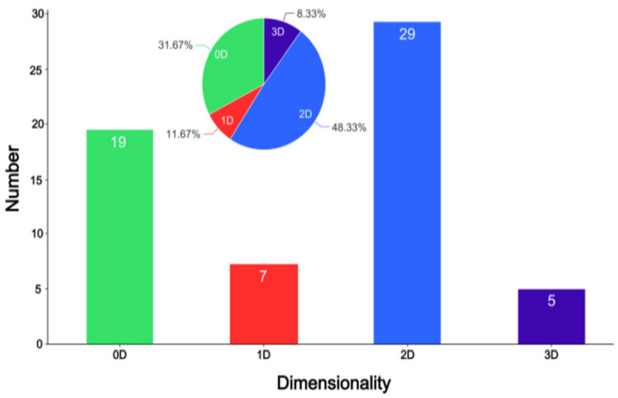

Fig. 2 Distribution of hydroxyborate with specific dimensionality of the B–O/OH anionic framework. Inset: corresponding proportion in %.

High-throughput data and crystal structure analysis

For the NCS hydroxyborates, our investigation focuses on key properties like band gaps, second-order NLO coefficients, and birefringence (optical anisotropy), all of which are essential for practical applications in NLO materials as shown in Table S6.† The birefringence Δn and the maximum SHG coefficients $|d_{ij}|^{\max}$ of hydroxyborates are plotted against their band gaps E_g-HSE06 in Fig. 4, respectively. The majority of the compounds exhibits large band gaps, ranging from 5.15 to 7.82 eV. A total of 30 compounds have large SHG coefficients $|d_{ij}|^{\max} \geq 0.39$ pm V^{-1} (1 × d_{36} (KDP)) and there are two compounds with 3D B–O/OH anionic frameworks, two with 1D infinite chains, seven with 0D isolated clusters, and nineteen with 2D infinite layers. $Na_2Ba_2(B_{10}O_{17}(OH)_2)$ has the largest SHG coefficient $|d_{22}|^{\max} = 1.08$ pm V^{-1} (2.8 × KDP) among the screened hydroxyborates, and exhibits a $^2[B_{10}O_{17}(OH)_2]_\infty$ infinite double layer. Further details of $Na_2Ba_2(B_{10}O_{17}(OH)_2)$ will be provided in the

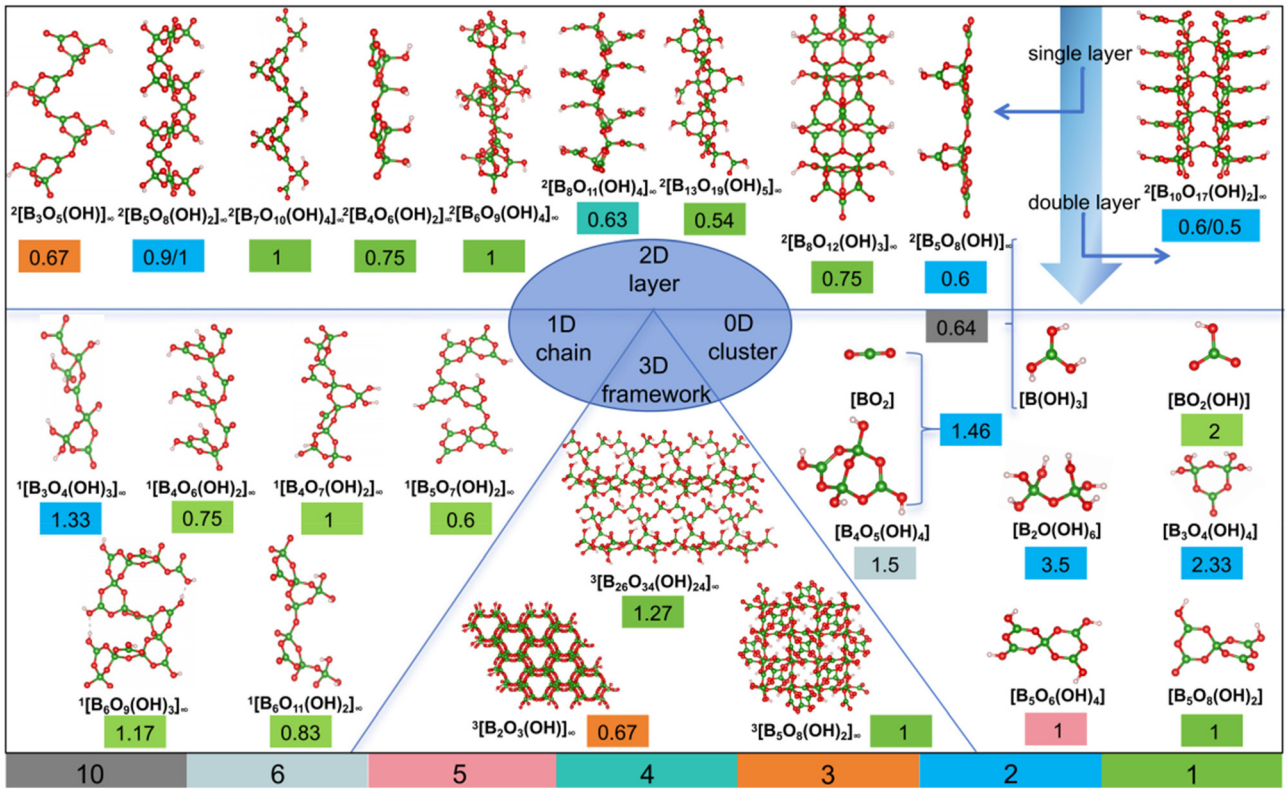

Fig. 3 Various dimensionalities of B–O/OH anionic frameworks, alongside the (A + OH)/B ratio among available hydroxyborates. The count in the final row depicts the quantity of existing hydroxyborates with an inherent ratio of (A + OH)/B through varied colors.

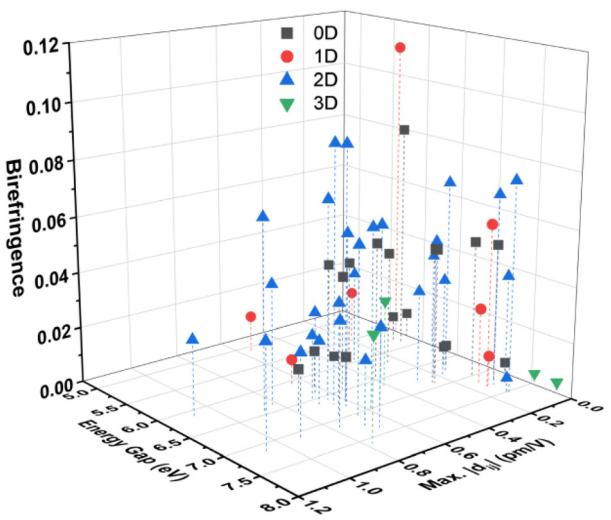

Fig. 4 Calculated E_g-HSE06 band gaps *vs.* the maximum SHG coefficients *vs.* birefringence at 1064 nm of typical hydroxyborates. Dimensionalities of B–O/OH anionic frameworks are distinguished by diverse icons.

following sections. A total of 26 compounds have moderate birefringences with $\Delta n \geq 0.040$ and there are two with 1D infinite chains, eight with 0D isolated clusters, and sixteen with 2D infinite layers. When the dimensionality of the B–O/OH anionic framework is 3, the largest birefringence is only 0.037 at 1064 nm. In contrast, when the dimensionality of the B–O/OH anionic framework is 0, 1, and 2, the respective largest birefringence values are 0.082 for $Ba(BO_2(OH))$, 0.110 for $Bi(B_4O_6(OH)_2)(OH)$, and 0.091 for $CaB_8O_{11}(OH)_4$ at 1064 nm. An optimized arrangement is conducive to optical anisotropy, thereby enhancing birefringence. When functional groups polymerize to form lower-dimensional structural frameworks, the arrangement can be optimized, which is favorable for producing appropriate birefringence. When functional groups polymerize to form 3D B–O/OH anionic frameworks, the arrangement tends to be less conducive to anisotropy, resulting in smaller birefringence. To assess the overall properties of the hydroxyborate system, we calculated the statistical averages of various linear and nonlinear optical characteristics. The average E_g-HSE06, Δn, and $|d_{ij}|^{max}$ are 6.71 eV, 0.040, and 0.39 pm V^{-1}, respectively. These findings suggest that the hydroxyborate system holds promise for NLO materials, exhibiting a combination of wide band gaps, moderate birefringence, and large SHG coefficients.

The selection of short-wavelength NLO crystals based on the following criteria is presented in Table S7†: E_g-HSE06 > 3.1 eV (λ_{cutoff} < 400 nm), the shortest PM wavelengths λ_{PM} < 400 nm, and $|d_{ij}|^{max} \geq 0.39$ pm V^{-1} ($1 \times d_{36}$ (KDP)). Notably, the materials satisfying the criteria are mainly alkali and alkaline-earth metal hydroxyborates including $Ba_2B_{13}O_{19}(OH)_5{\cdot}5H_2O$,[59] $CaB_8O_{11}(OH)_4$,[60]

$SrB_8O_{11}(OH)_4$,[60] $Li_2CsB_7O_{10}(OH)_4$,[61] $Na_2B_5O_8(OH)\cdot 2H_2O$,[62] and $K_3B_3O_4(OH)_4\cdot 2H_2O$.[63] The optical properties we calculated are consistent with the reported results,[59–63] confirming the reliability and accuracy of our computational methods.

Hydroxyborates have been extensively investigated as NLO materials. Five crystals, namely $KCa_4(B_{22}O_{32})(OH)_{10}Cl\cdot 4H_2O$,[64,65] $Ca_9B_{26}O_{34}(OH)_{24}Cl_4\cdot 13H_2O$,[66] $Na_2Ba_2(B_{10}O_{17}(OH)_2)$,[67] $Na_4(B_{10}O_{16}(OH)_2)\cdot 4H_2O$,[68] and $(Na(H_2O))_2(B_5O_8(OH))$[69] are identified as novel NLO materials with unreported NLO properties. Their predicted properties are listed in Table S8.†

$KCa_4(B_{22}O_{32})(OH)_{10}Cl\cdot 4H_2O$. $KCa_4(B_{22}O_{32})(OH)_{10}Cl\cdot 4H_2O$ is a natural mineral with the crystal structure determined by Rastsvetaeva *et al.* (1992)[65] (ICSD. 39637). The structure was refined by Poulin and Grice (2013)[64] (ICSD. 39637). It exhibits a large band gap of 7.08 eV, a relatively large SHG coefficient d_{12} = 0.59 pm V^{-1} (1.5 × KDP), and a birefringence of 0.065@1064 nm. This compound crystallizes in the *P*1 space group and features a $^2[B_5O_8(OH)]_\infty$ layered structure along the *ac*-plane containing $[BO_3]$, $[BO_2(OH)]$, and $[BO_4]$ polyhedra. $[B(OH)_3]$ polyhedra are isolated from the borate sheets and shown in Fig. 5a. The layered feature and triangular hydroxyborate anionic groups can result in moderate birefringence, and the shortest PM wavelength λ_{PM} can reach 235 nm, which expands into the solar blind region (200–280 nm).

$Ca_9B_{26}O_{34}(OH)_{24}Cl_4\cdot 13H_2O$. It crystallizes in the *P*1 space group and features a 3D structure with the $(OH)^-$ located at the triangular $[BO_2(OH)]$, the tetrahedral $[BO_2(OH)_2]$ and $[BO_3(OH)]$ anionic groups as shown in Fig. 5b. It exhibits a small birefringence of 0.031@1064 nm, although it has a large band gap of 6.65 eV and an SHG coefficient d_{24} = 0.41 pm V^{-1} (1.1 × KDP) attributed to the polarity favorable arrangement of $[BO_3]$ triangles. The reason for the small birefringence is the locally small structural anisotropy of the tetrahedral $[BO_2(OH)_2]$ and $[BO_3(OH)]$. The shortest PM wavelength λ_{PM} is 336 nm, implying that PM capability extends into the long-wave ultraviolet region (320–400 nm).

$Na_2Ba_2(B_{10}O_{17}(OH)_2)$. It exhibits a $^2[B_{10}O_{17}(OH)_2]_\infty$ infinite double layer along the *ab*-plane, crystallizing in the monoclinic space group *C*2 as depicted in Fig. 5c. It has a moderate band gap of 6.12 eV and the largest SHG coefficient d_{22} = 1.08 pm V^{-1} (2.8 × KDP) among the screened hydroxyborates, but exhibits a small birefringence of 0.027@1064 nm. The shortest PM wavelengths λ_{PM} is 367 nm, implying that PM capability extends into the long-wave ultraviolet region (320–400 nm).

$Na_4(B_{10}O_{16}(OH)_2)\cdot 4H_2O$. $Na_4(B_{10}O_{16}(OH)_2)\cdot 4H_2O$ crystallizes in the monoclinic *Pc* space group. The structure features a $^2[B_5O_8(OH)]_\infty$ infinite single layer along the *ab*-plane with the $(OH)^-$ located at the tetrahedral $[BO_2(OH)]$ anionic groups as shown in Fig. 5d. It shows a large band gap of 6.42 eV. Owing to the polarity-favorable arrangement of $[BO_3]$ and $[BO_2(OH)]$ triangles, $Na_4(B_{10}O_{16}(OH)_2)(H_2O)_4$ has a large SHG coefficient d_{11} = 0.66 pm V^{-1} (1.7 × KDP). The birefringence is 0.03 at 1064 nm. Its smaller birefringence results in a longer λ_{PM} = 318 nm due to the locally small structural anisotropy of the

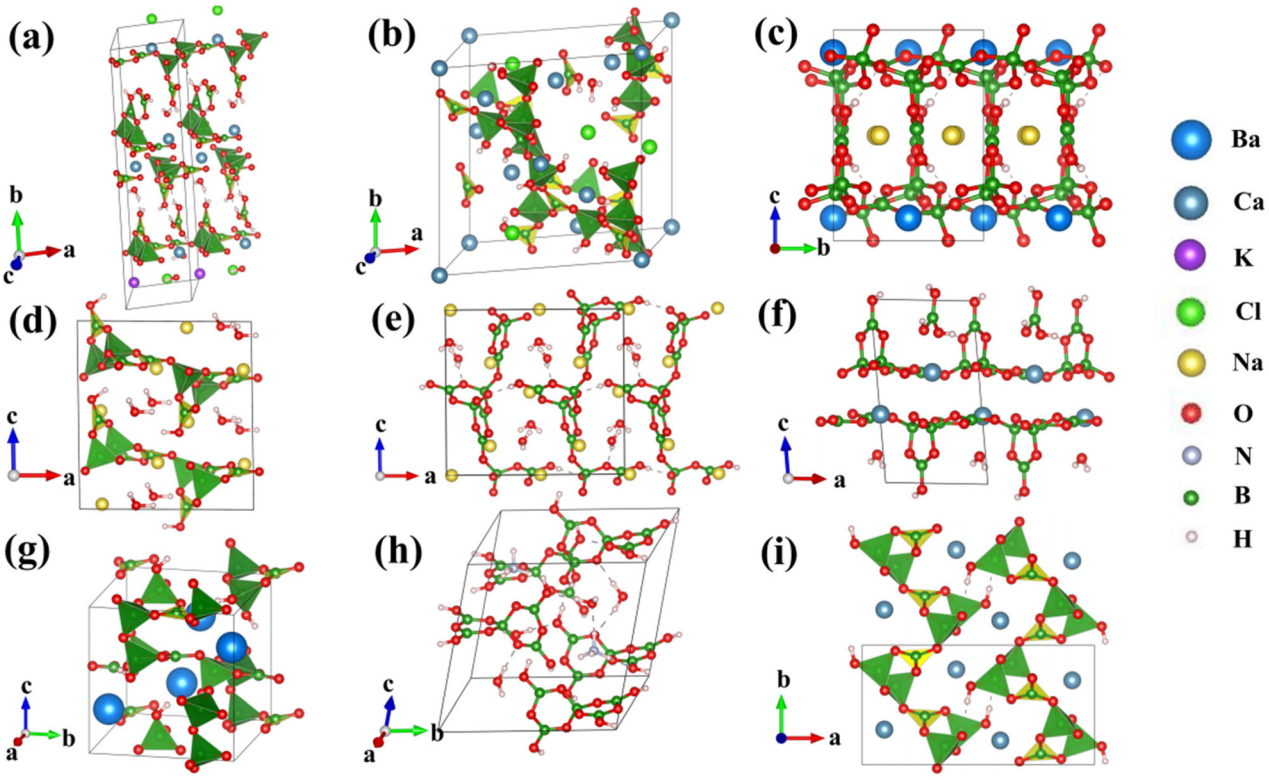

Fig. 5 Crystal structures of (a) $KCa_4(B_{22}O_{32})(OH)_{10}Cl\cdot 4H_2O$, (b) $Ca_9B_{26}O_{34}(OH)_{24}Cl_4\cdot 13H_2O$, (c) $Na_2Ba_2(B_{10}O_{17}(OH)_2)$, (d) $Na_4(B_{10}O_{16}(OH)_2)\cdot 4H_2O$, (e) $(Na(H_2O))_2(B_5O_8(OH))$, (f) $Ca_2(B_5O_8(OH))_2B(OH)_3\cdot H_2O$, (g) $Ba_2(B_6O_9(OH)_4)$, (h) $NH_4(B_5O_6(OH)_4)\cdot 2H_2O$, and (i) $CaB_3O_5(OH)$.

tetrahedral [BO_4], implying that the PM capability extends into the medium-wave ultraviolet region (280–320 nm).

$(Na(H_2O))_2(B_5O_8(OH))$. $(Na(H_2O))_2(B_5O_8(OH))$ and $Na_4(B_{10}O_{16}(OH)_2)(H_2O)_4$ have the same $^2[B_5O_8(OH)]_\infty$ infinite single layer, but $(Na(H_2O))_2(B_5O_8(OH))$ belongs to the orthorhombic $Pna2_1$ space group with an infinite single layer along the *bc*-plane as shown in Fig. 5e. It exhibits a large band gap of 6.47 eV and a birefringence of 0.023@1064 nm with an SHG coefficient d_{33} = −0.66 pm V^{-1} (1.7 × KDP). The shortest PM wavelength λ_{PM} = 345 nm indicates its PM capability in the long-wave ultraviolet region (320–400 nm).

Besides the above five crystals, four hydroxyborates—$Ca_2(B_5O_8(OH))_2B(OH)_3{\cdot}H_2O$,[70] $Ba_2(B_6O_9(OH)_4)$,[71] $NH_4(B_5O_6(OH)_4){\cdot}2H_2O$,[72] and $CaB_3O_5(OH)$[73]—are recognized as potential NLO materials as shown in Fig. 5f, g, h, i, and Table S8.† These crystals have only been partially characterized, and some optical properties such the PM wavelengths have not been reported.

$Ca_2(B_5O_8(OH))_2B(OH)_3{\cdot}H_2O$ shows a wide band gap of 7.38 eV with a moderate birefringence of 0.071@1064 nm. The d_{12} coefficient is about −0.67 pm V^{-1} (1.7 × KDP), which is consistent with the measured powder SHG response (1.8 × KDP).[70] λ_{PM} was calculated to be about 229 nm, implying that the PM capability extends into the solar blind region (200–280 nm). Considering the excellent multiple properties, large-size crystals should be grown for further evaluation. **$Ba_2(B_6O_9(OH)_4)$** shows a band gap of 7.14 eV and the d_{22} coefficient is about 1.07 pm V^{-1} (2.8 × KDP). The calculated results are consistent with the measured powder SHG response (3 × KDP) and UV cutoff edge (<190 nm).[71] It exhibits a birefringence of 0.037 at 1064 nm. The shortest PM wavelength λ_{PM} is 302 nm, which extends into the medium-wave ultraviolet region (280–320 nm). **$NH_4(B_5O_6(OH)_4){\cdot}2H_2O$** achieves a balance among the band gap, birefringence, and the SHG coefficient, being 6.47 eV, 0.050 at 1064 nm, and d_{12} = −0.39 pm V^{-1} (1.0 × KDP), respectively. P. Becker *et al.* reported the linear optical effect, a suitable birefringence of 0.058 at 1064 nm and a UV cutoff edge of less than 180 nm.[72] The calculated results are in good agreement with the reported results, fully demonstrating the rationality and reliability of the calculation methods. λ_{PM} can reach 240 nm, implying that the PM capability extends into the solar blind region (200–280 nm), and the NLO effect with large-size crystals should be evaluated. **$CaB_3O_5(OH)$** is another typical hydroxyborate. It has a wide band gap of 7.15 eV. The d_{33} coefficient is about −0.77 pm V^{-1} (1.9 × KDP). Its birefringence is Δn = 0.037@1064 nm and λ_{PM} is 327 nm, and extends into the long-wave ultraviolet region (320–400 nm).

From the analyzed results, it is found that the PM capability of $KCa_4(B_{22}O_{32})(OH)_{10}Cl{\cdot}4H_2O$, $Ca_2(B_5O_8(OH))_2B(OH)_3{\cdot}H_2O$, and $NH_4(B_5O_6(OH)_4){\cdot}2H_2O$ extend into the solar blind region. Additionally, $Na_4(B_{10}O_{16}(OH)_2){\cdot}4H_2O$ and $Ba_2(B_6O_9(OH)_4)$ are identified as potential SHG materials suitable for the range of the medium-wave ultraviolet region. Furthermore, $Ca_9B_{26}O_{34}(OH)_{24}Cl_4{\cdot}13H_2O$, $Na_2Ba_2(B_{10}O_{17}(OH)_2)$, $(Na(H_2O))_2(B_5O_8(OH))$, and $CaB_3O_5(OH)$ are recognized as potential SHG materials for the range of the long-wave ultraviolet region.

Optics-related properties

Most of the hydroxyborates screened exhibit large band gaps, and half of them have strong SHG effects, yet they exhibit different birefringence values. In order to investigate the origin of the difference in birefringence, we analyzed the influence of the anionic framework, the arrangement and the density of anionic groups, particularly the π-conjugated [BO_3], [$B(OH)_3$], and [$BO_2(OH)$] units. As we all know, the terminal positions of $(OH)^-$ groups and the presence of A cations can cut off the anionic framework, as scissors. As shown in Fig. 6a, the hydroxyborates with a birefringence $\Delta n \geq 0.05$@1064 nm mainly exhibit the low-dimensional B–O/OH anionic framework, owing to the structural anisotropy. However, for birefringence $\Delta n < 0.05$@1064 nm, the compounds show 0D to 3D anionic frameworks. In addition to the dimensions of the anionic framework as a birefringence-descriptor, the arrangement and density of anionic groups, particularly the π-conjugated [BO_3], [$B(OH)_3$], and [$BO_2(OH)$] units should be considered. Therefore, we analyzed the compounds with 2D anionic frameworks and (A + OH)/B ∼ 0.6; the birefringence changes from 0.005 to 0.076@1064 nm, as shown in Fig. 6b. The densities of [BO_3], [$B(OH)_3$], and [$BO_2(OH)$] units in $Ca_2(B_5O_8(OH))_2B(OH)_3{\cdot}H_2O$-I (Ca-I), $Ca_2(B_5O_8(OH))_2(B(OH)_3){\cdot}H_2O$-II (Ca-II), $Ca_2(B_5O_8(OH))_2(B(OH)_3){\cdot}H_2O$-III (Ca-III), $Sr_2(B_5O_8(OH))_2(B(OH)_3){\cdot}H_2O$-I (Sr-I), $Sr_2(B_5O_8(OH))_2(B(OH)_3){\cdot}H_2O$-II (Sr-II), $Sr_2(B_5O_8(OH))_2(B(OH)_3){\cdot}H_2O$-III (Sr-III), $Ba_2(B_5O_8(OH))_2(B(OH)_3){\cdot}H_2O$-I (Ba-I), and $Ba_2B_{10}O_{16}(OH)_2(H_3BO_3){\cdot}H_2O$-II (Ba-II) are 0.0168, 0.0181, 0.0181, 0.0162, 0.0162, 0.0111, 0.0163, and 0.0174 $Å^{-3}$, respectively. As can be seen from Fig. 6b, for Sr-III, the density of [BO_3], [$B(OH)_3$], and [$BO_2(OH)$] units is small, about 0.0111 $Å^{-3}$, and the birefringence is also very low, about 0.005 at 1064 nm. As the density of the π-conjugated units increases, the birefringence also increases. When the density of the π-conjugated units is at its maximum of 0.0181 $Å^{-3}$, the birefringence of Ca-II and Ca-III is 0.071 and 0.075, respectively, at 1064 nm. The slight difference in birefringence for Ca-II and Ca-III is mainly attributed to the different arrangements. In addition, the different chemical compositions and the arrangement should also be considered; taking Sr-II and Ba-I as the example, they have

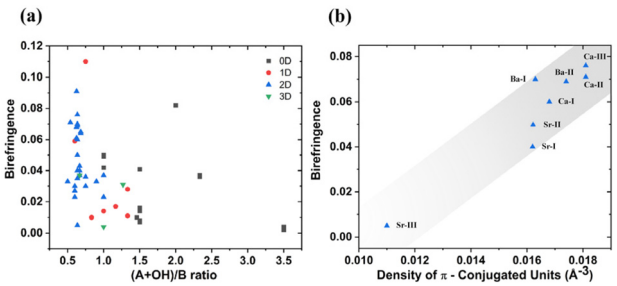

Fig. 6 (a) Birefringence at 1064 nm *versus* (A + OH)/B ratio among the screened hydroxyborates. (b) Birefringence at 1064 nm *versus* density of π-conjugated [BO_3], [$B(OH)_3$], and [$BO_2(OH)$] units, taking the (A + OH)/B ratio of 0.636 as the example.

different birefringence values of 0.050 and 0.070 at 1064 nm with similar π-conjugated unit density values of 0.0162 and 0.0163 Å^{-3}.

Leveraging high-throughput screening strategies, we screened out compounds exhibiting balanced NLO performance in the hydroxyborate system. Representative compounds, such as $KCa_4(B_{22}O_{32})(OH)_{10}Cl{\cdot}4H_2O$, are selected for elucidating their electronic structures and investigating the origin of their strong SHG effects and moderate birefringence.

The NLO properties of $KCa_4(B_{22}O_{32})(OH)_{10}Cl{\cdot}4H_2O$ are thoroughly investigated, as depicted in Fig. S1.† Examination of the band structures (Fig. S1a†) reveals that $KCa_4(B_{22}O_{32})(OH)_{10}Cl{\cdot}4H_2O$ is characterized as a direct-band-gap material. Analysis of the total and partial density of states (PDOS) indicates that the valence bands (VBs) predominantly derive from O-p, B-p, H-s, and Cl-p orbitals, while the conduction bands (CBs) are primarily constituted by B-p, O-p, and H-s orbitals. The hybridization of sp orbitals from B, O, and OH on both sides of the band gap, as revealed by PDOS, signifies the strong covalent bonding within the hydroxyborate anionic frameworks. The band-resolved analysis of SHG (Fig. S1b†) corroborates that the predominant contributions to the optical properties stem from the hydroxyborate anionic groups, aligning well with anionic group theory. Additionally, the SHG-weighted density is utilized to delve deeper into the contribution of atoms or groups to the SHG response, employing the sum-over-states method implemented in the CASTEP code. Based on these contributions, the SHG-density method can be divided into the occupied and unoccupied states of VE and VH, respectively. In the case of $KCa_4(B_{22}O_{32})(OH)_{10}Cl{\cdot}4H_2O$, particular emphasis is placed on plotting the VE processes due to their significant contributions to the SHG response, as depicted in Fig. S1c.† The primary VE process indicates that $[B(OH)_3]$, $^2[B_5O_8(OH)]_\infty$, Cl, and Ca in occupied states, along with B–O/OH anionic groups and Ca in unoccupied states, are the primary contributors to the SHG effects. Overall, this finding aligns with our comprehension of the structure–property relationship in hydroxyborates.

The $KCa_4(B_{22}O_{32})(OH)_{10}Cl{\cdot}4H_2O$ compound features an anionic arrangement of $^2[B_5O_8(OH)]_\infty$ and $[B(OH)_3]$, with an (A + OH)/B ratio of 0.682. Given this ratio, the moderate birefringence of the compound can be anticipated. Based on the calculated refractive indices and dispersion curves as plotted in Fig. 7a, $KCa_4(B_{22}O_{32})(OH)_{10}Cl{\cdot}4H_2O$ has a calculated birefringence of 0.065@1064 nm, and the shortest PM wavelength of $KCa_4(B_{22}O_{32})(OH)_{10}Cl{\cdot}4H_2O$ is determined according to the condition $n_{max}(2\lambda) = n_{min}(\lambda)$ for the type-I PM process. The shortest PM wavelength is about 235 nm, suggesting its potential for the output PM SHG ultraviolet light. To ascertain the contribution to birefringence, the response electron distribution anisotropy (REDA) approximation was employed.[74] From Table S10,† it can be concluded that the $[BO_3]$ units in $KCa_4(B_{22}O_{32})(OH)_{10}Cl{\cdot}4H_2O$ contribute most significantly, showing a value of 52.46%. Meanwhile $[BO_2(OH)]$, $[B(OH)_3]$, and $[BO_4]$ units contribute relatively small percentages of 26.55, 14.28, and 4.04%, respectively. Overall, $^2[B_5O_8(OH)]_\infty$ layers and $[B(OH)_3]$ clusters contribute significantly to producing large optical anisotropy, thereby generating moderate birefringence. Moreover, the electron density distribution of $KCa_4(B_{22}O_{32})(OH)_{10}Cl{\cdot}4H_2O$ is clearly visualized in Fig. 7b. Obviously, the anisotropic electronic distribution of $^2[B_5O_8(OH)]_\infty$ layers and $[B(OH)_3]$ clusters results in the moderate birefringence, well consistent with the REDA result.

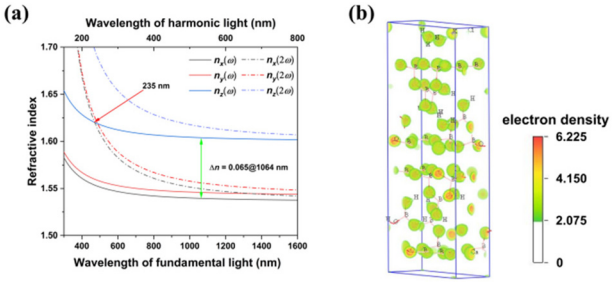

Fig. 7 (a) Refractive index and PM property evaluation. (b) Electron density distribution of $KCa_4(B_{22}O_{32})(OH)_{10}Cl{\cdot}4H_2O$.

Conclusions

In pursuit of identifying promising short-wavelength NLO materials, especially in the solar blind region (200–280 nm), our study focused on the hydroxyborate system utilizing first-principles high-throughput screening. We systematically assessed over 222 NCS hydroxyborate compounds from 718 hydroxyborate compounds in the ICSD. Through meticulous compound screening, structural optimization, property simulation, and mechanism analysis, we identified several promising SHG materials in different operational wavelength. In the solar blind region (200–280 nm), compounds such as $KCa_4(B_{22}O_{32})(OH)_{10}Cl{\cdot}4H_2O$, $Ca_2(B_5O_8(OH))_2B(OH)_3{\cdot}H_2O$, and $NH_4(B_5O_6(OH)_4){\cdot}2H_2O$ have shown potential. Notably, the PM wavelengths for these three compounds are all less than 266 nm. For the medium-wave ultraviolet region (280–320 nm), $Na_4(B_{10}O_{16}(OH)_2){\cdot}4H_2O$ and $Ba_2(B_6O_9(OH)_4)$ have been identified as suitable candidates. Additionally, in the long-wave ultraviolet region (320–400 nm), $Ca_9B_{26}O_{34}(OH)_{24}Cl_4{\cdot}13H_2O$, $Na_2Ba_2(B_{10}O_{17}(OH)_2)$, $(Na(H_2O))_2(B_5O_8(OH))$, and $CaB_3O_5(OH)$ have been recognized as potential materials. Our calculated properties align well with the reported findings, thereby showcasing the precision and reliability of our calculation methods. The investigation of hydroxyborates in relation to their birefringence, the dimensionality of the B–O/OH anionic framework, and the (A + OH)/B ratio may reveal hydroxyborates with short PM wavelengths, which are desirable for NLO applications. Additionally, we have noted that a moderate birefringence is observed when the (A + OH)/B ratio is approximately 0.6. Specifically, the phenomenon is notably pronounced in 2D anionic layers and 1D anionic chains, exhibiting a birefringence value of 0.05 or greater at a wavelength of 1064 nm. Additionally, when the (A + OH)/B ratio is 1 or 2, a higher like-

lihood of moderate birefringence is observed in 0D anionic clusters. This study provides novel insights and strategies for tailoring the birefringent properties of materials. It is expected to facilitate the advancement and exploration of promising short-wavelength NLO materials within the hydroxyborate system.

Author contributions

Zhihua Yang: research design, methodology, funding acquisition, and writing – review & editing. Shilie Pan: research design, funding acquisition, and writing – review & editing. Chenxu Li: research design, investigation, theoretical calculations, and original draft preparation. Abudukadi Tudi: research design, investigation, and formal analysis. Huanhuan Cheng: research design, methodology, and formal analysis. Qingyu Liu: investigation and software development.

Data availability

The data supporting this article have been included as part of the ESI.†

Conflicts of interest

There are no conflicts to declare.

Acknowledgements

This work is supported by the Key Research Program of Frontier Sciences, CAS (ZDBS-LY-SLH035), the National Natural Science Foundation of China (22193044, 22361132544, 22335007, and 52202014), the National Key R&D Program of China (2021YFB3601502), Natural Science Foundation of Xinjiang (2021D01E05 and 2021D01B103), the Xinjiang Major Science and Technology Project (2021A01001), Tianshan Basic Research Talents (2022TSYCJU0001), and CAS Project for Young Scientists in Basic Research (YSBR-024).

References

1 P. A. Franken, A. E. Hill, C. W. Peters and G. Weinreich, Generation of optical harmonics, *Phys. Rev. Lett.*, 1961, **7**, 118–119.
2 X. Liu, P. Gong, Y. Yang, G. Song and Z. Lin, Nitrate nonlinear optical crystals: A survey on structure-performance relationships, *Coord. Chem. Rev.*, 2019, **400**, 213045.
3 S.-P. Guo, Y. Chi and G.-C. Guo, Recent achievements on middle and far-infrared second-order nonlinear optical materials, *Coord. Chem. Rev.*, 2017, **335**, 44–57.
4 T. T. Tran, H. Yu, J. M. Rondinelli, K. R. Poeppelmeier and P. S. Halasyamani, Deep ultraviolet nonlinear optical materials, *Chem. Mater.*, 2016, **28**, 5238–5258.
5 Y. Wang and S. Pan, Recent development of metal borate halides: Crystal chemistry and application in second-order NLO materials, *Coord. Chem. Rev.*, 2016, **323**, 15–35.
6 M. Wu, E. Tikhonov, A. Tudi, I. Kruglov, X. Hou, C. Xie, S. Pan and Z. Yang, Target–driven design of deep–UV nonlinear optical materials via interpretable machine learning, *Adv. Mater.*, 2023, **35**, 2300848.
7 E. Timurdogan, C. V. Poulton, M. J. Byrd and M. R. Watts, Electric field-induced second-order nonlinear optical effects in silicon waveguides, *Nat. Photonics*, 2017, **11**, 200–206.
8 Y. Yang, X. Dong, Z. Yang and S. Pan, $CsBaB_9O_{15}$: a high performance ultraviolet nonlinear optical material activated by the peculiar double layered configuration, *Sci. Bull.*, 2021, **66**, 2165–2169.
9 Y. Xia, C. Chen, D. Tang and B. Wu, New nonlinear optical crystals for UV and VUV harmonic generation, *Adv. Mater.*, 1995, **7**, 79–81.
10 J. Zhang, C. Wu, H. Shi, C. Xie, Z. Yang and S. Pan, An interlinked prediction-experiment paradigm discovering deep-ultraviolet fluorooxoborates with desired optical nonlinearity and birefringence, *Matter*, 2023, **6**, 1188–1202.
11 J. Jiao, M. Zhang and S. Pan, Aluminoborates as nonlinear optical materials, *Angew. Chem., Int. Ed.*, 2023, **62**, e202217037.
12 G. Shi, Y. Wang, F. Zhang, B. Zhang, Z. Yang, X. Hou, S. Pan and K. R. Poeppelmeier, Finding the next deep-ultraviolet nonlinear optical material: $NH_4B_4O_6F$, *J. Am. Chem. Soc.*, 2017, **139**, 10645–10648.
13 X. Wang, Y. Wang, B. Zhang, F. Zhang, Z. Yang and S. Pan, CsB_4O_6F: A congruent–melting deep–ultraviolet nonlinear optical material by combining superior functional units, *Angew. Chem., Int. Ed.*, 2017, **56**, 14119–14123.
14 B. Zhang, G. Shi, Z. Yang, F. Zhang and S. Pan, Fluorooxoborates: Beryllium–free deep–ultraviolet nonlinear optical materials without layered growth, *Angew. Chem., Int. Ed.*, 2017, **56**, 3916–3919.
15 M. Mutailipu, M. Zhang, H. Wu, Z. Yang, Y. Shen, J. Sun and S. Pan, $Ba_3Mg_3(BO_3)_3F_3$ polymorphs with reversible phase transition and high performances as ultraviolet nonlinear optical materials, *Nat. Commun.*, 2018, **9**, 3089.
16 M. Mutailipu, M. Zhang, B. Zhang, L. Wang, Z. Yang, X. Zhou and S. Pan, $SrB_5O_7F_3$ functionalized with $[B_5O_9F_3]^{6-}$ chromophores: Accelerating the rational design of deep–ultraviolet nonlinear optical materials, *Angew. Chem., Int. Ed.*, 2018, **57**, 6095–6099.
17 Y. Wang, B. Zhang, Z. Yang and S. Pan, Cation–tuned synthesis of fluorooxoborates: Towards optimal deep–ultraviolet nonlinear optical materials, *Angew. Chem., Int. Ed.*, 2018, **57**, 2150–2154.
18 W. Cai, A. Abudurusuli, C. Xie, E. Tikhonov, J. Li, S. Pan and Z. Yang, Toward the rational design of mid–infrared nonlinear optical materials with targeted properties via a

multi–level data–driven approach, *Adv. Funct. Mater.*, 2022, **32**, 2200231.
19 B.-H. Lei, S. Pan, Z. Yang, C. Cao and D. J. Singh, Second harmonic generation susceptibilities from symmetry adapted wannier functions, *Phys. Rev. Lett.*, 2020, **125**, 187402.
20 F. Li, W. Jin, R. An, M. Mutailipu, S. Pan and Z. Yang, Covalently bonded fluorine optimizing deep-ultraviolet nonlinear optical performance of fluorooxoborates, *Sci. Bull.*, 2024, **69**, 1192–1196.
21 M. Mutailipu, K. R. Poeppelmeier and S. Pan, Borates: A rich source for optical materials, *Chem. Rev.*, 2021, **121**, 1130–1202.
22 T. T. Tran, J. Young, J. M. Rondinelli and P. S. Halasyamani, Mixed-metal carbonate fluorides as deep-ultraviolet nonlinear optical materials, *J. Am. Chem. Soc.*, 2017, **139**, 1285–1295.
23 G. Zou, N. Ye, L. Huang and X. Lin, Alkaline-alkaline earth fluoride carbonate crystals $ABCO_3F$ (A = K, Rb, Cs; B = Ca, Sr, Ba) as nonlinear optical materials, *J. Am. Chem. Soc.*, 2011, **133**, 20001–20007.
24 G. Peng, C. Lin and N. Ye, $NaZnCO_3(OH)$: A high-performance carbonate ultraviolet nonlinear optical crystal derived from $KBe_2BO_3F_2$, *J. Am. Chem. Soc.*, 2020, **142**, 20542–20546.
25 X. Liu, L. Kang, P. Gong and Z. Lin, $LiZn(OH)CO_3$: A deep-ultraviolet nonlinear optical hydroxycarbonate designed from a Diamond-like structure, *Angew. Chem., Int. Ed.*, 2021, **60**, 13574–13578.
26 S. Zhao, Y. Yang, Y. Shen, B. Zhao, L. Li, C. Ji, Z. Wu, D. Yuan, Z. Lin, M. Hong and J. Luo, Cooperation of three chromophores generates the water–resistant nitrate nonlinear optical material $Bi_3TeO_6OH(NO_3)_2$, *Angew. Chem., Int. Ed.*, 2017, **56**, 540–544.
27 X. Dong, L. Huang, C. Hu, H. Zeng, Z. Lin, X. Wang, K. M. Ok and G. Zou, $CsSbF_2SO_4$: An excellent ultraviolet nonlinear optical sulfate with a $KTiOPO_4$ (KTP)–type structure, *Angew. Chem., Int. Ed.*, 2019, **58**, 6528–6534.
28 L. Li, Y. Wang, B. Lei, S. Han, Z. Yang, K. R. Poeppelmeier and S. Pan, A new deep-utraviolet transparent orthophosphate $LiCs_2PO_4$ with large second harmonic generation response, *J. Am. Chem. Soc.*, 2016, **138**, 9101–9104.
29 S. Cho and K. M. Ok, $LiRE(SO_4)_2$(RE = Y, Gd, Eu): noncentrosymmetric chiral rare-earth sulfates with very large band gaps, *Mater. Chem. Front.*, 2023, **7**, 65–71.
30 H. Wu, B. Zhang, H. Yu, Z. Hu, J. Wang, Y. Wu and P. S. Halasyamani, Designing silicates as deep-UV nonlinear optical (NLO) materials using edge-sharing tetrahedra, *Angew. Chem., Int. Ed.*, 2020, **59**, 8922–8926.
31 Y.-F. Shi, Z. Ma, B.-X. Li, X.-T. Wu, H. Lin and Q.-L. Zhu, Phase matching achieved by isomorphous substitution in IR nonlinear optical material $Ba_2SnSSi_2O_7$with an undiscovered $[SnO_4S]$ functional motif, *Mater. Chem. Front.*, 2022, **6**, 3054–3061.
32 D. Chu, Y. Huang, C. Xie, E. Tikhonov, I. Kruglov, G. Li, S. Pan and Z. Yang, Unbiased screening of novel infrared nonlinear optical materials with high thermal conductivity: Long-neglected nitrides and popular chalcogenides, *Angew. Chem., Int. Ed.*, 2023, **62**, e202300581.
33 C. T. Chen, G. L. Wang, X. Y. Wang and Z. Y. Xu, Deep-UV nonlinear optical crystal $KBe_2BO_3F_2$–discovery, growth, optical properties and applications, *Appl. Phys. B*, 2009, **97**, 9–25.
34 C. T. Chen, B. C. Wu, A. D. Jiang and G. M. You, A new-type ultraviolet SHG crystal β-BaB_2O_4, *Sci. Sin., Ser. B (Engl. Ed.)*, 1985, **28**, 235–243.
35 C. Chen, Y. Wu, A. Jiang, B. Wu, G. You, R. Li and S. Lin, New nonlinear-optical crystal: LiB_3O_5, *J. Opt. Soc. Am. B*, 1989, **6**, 616.
36 Y. Mori, S. Nakajima, A. Miyamoto, M. Inagaki, T. Sasaki, H. Yoshida and S. Nakai, in *Solid State Lasers for Application to Inertial Confinement Fusion (ICF)*, ed. M. Andre and H. T. Powell, SPIE, 1995.
37 M. Cheng, X. Hou, Z. Yang and S. Pan, Recent progress in borate-based short-wavelength nonlinear optical crystals with boron-oxygen skeleton modification, *Mater. Chem. Front.*, 2023, **7**, 4683–4692.
38 Y. Gan, N. Miao, P. Lan, J. Zhou, S. R. Elliott and Z. Sun, Robust design of high-performance optoelectronic chalcogenide crystals from high-throughput computation, *J. Am. Chem. Soc.*, 2022, **144**, 5878–5886.
39 X.-Y. Ma, J. P. Lewis, Q.-B. Yan and G. Su, Accelerated discovery of two-dimensional optoelectronic octahedral oxyhalides via high-throughput ab initio calculations and machine learning, *J. Phys. Chem. Lett.*, 2019, **10**, 6734–6740.
40 S. R. Foltyn, L. Civale, J. L. MacManus-Driscoll, Q. X. Jia, B. Maiorov, H. Wang and M. Maley, Materials science challenges for high-temperature superconducting wire, *Nat. Mater.*, 2007, **6**, 631–642.
41 A. Gurevich, Challenges and opportunities for applications of unconventional superconductors, *Annu. Rev. Condens. Matter Phys.*, 2014, **5**, 35–56.
42 A. Jain, S. P. Ong, G. Hautier, W. Chen, W. D. Richards, S. Dacek, S. Cholia, D. Gunter, D. Skinner, G. Ceder and K. A. Persson, Commentary: The Materials Project: A materials genome approach to accelerating materials innovation, *APL Mater.*, 2013, **1**, 011002.
43 G. Bergerhoff, I. Brown and F. Allen, *International Union of Crystallography*, Chester, England, 1987.
44 P. Geerlings, F. De Proft and W. Langenaeker, Conceptual density functional theory, *Chem. Rev.*, 2003, **103**, 1793–1874.
45 S. J. Clark, M. D. Segall, C. J. Pickard, P. J. Hasnip, M. I. J. Probert, K. Refson and M. C. Payne, First principles methods using CASTEP, *Z. Kristallogr. – Cryst. Mater.*, 2005, **220**, 567–570.
46 J. P. Perdew, K. Burke and M. Ernzerhof, Generalized gradient approximation made simple, *Phys. Rev. Lett.*, 1997, **78**, 1396–1396.
47 A. M. Rappe, K. M. Rabe, E. Kaxiras and J. D. Joannopoulos, Optimized pseudopotentials, *Phys. Rev. B: Condens. Matter Mater. Phys.*, 1990, **41**, 1227–1230.

48 J. S. Lin, A. Qteish, M. C. Payne and V. Heine, Optimized and transferable nonlocal separable ab initio pseudopotentials, *Phys. Rev. B: Condens. Matter Mater. Phys.*, 1993, **47**, 4174–4180.

49 J. Heyd, G. E. Scuseria and M. Ernzerhof, Hybrid functionals based on a screened Coulomb potential, *J. Chem. Phys.*, 2003, **118**, 8207–8215.

50 W. Jia, J. Fu, Z. Cao, L. Wang, X. Chi, W. Gao and L.-W. Wang, Fast plane wave density functional theory molecular dynamics calculations on multi-GPU machines, *J. Comput. Phys.*, 2013, **251**, 102–115.

51 W. Jia, Z. Cao, L. Wang, J. Fu, X. Chi, W. Gao and L.-W. Wang, The analysis of a plane wave pseudopotential density functional theory code on a GPU machine, *Comput. Phys. Commun.*, 2013, **184**, 9–18.

52 D. R. Hamann, Optimized norm-conserving Vanderbilt pseudopotentials, *Phys. Rev. B: Condens. Matter Mater. Phys.*, 2013, **88**, 085117.

53 M. Schlipf and F. Gygi, Optimization algorithm for the generation of ONCV pseudopotentials, *Comput. Phys. Commun.*, 2015, **196**, 36–44.

54 A. V. Krukau, O. A. Vydrov, A. F. Izmaylov and G. E. Scuseria, Influence of the exchange screening parameter on the performance of screened hybrid functionals, *J. Chem. Phys.*, 2006, **125**, 224106.

55 C. Aversa and J. E. Sipe, Nonlinear optical susceptibilities of semiconductors: Results with a length-gauge analysis, *Phys. Rev. B: Condens. Matter Mater. Phys.*, 1995, **52**, 14636–14645.

56 S. N. Rashkeev, W. R. L. Lambrecht and B. Segall, Efficientab initiomethod for the calculation of frequency-dependent second-order optical response in semiconductors, *Phys. Rev. B: Condens. Matter Mater. Phys.*, 1998, **57**, 3905–3919.

57 B. Zhang, M.-H. Lee, Z. Yang, Q. Jing, S. Pan, M. Zhang, H. Wu, X. Su and C.-S. Li, Simulated pressure-induced blue-shift of phase-matching region and nonlinear optical mechanism for $K_3B_6O_{10}X$ (X = Cl, Br), *Appl. Phys. Lett.*, 2015, **106**, 031906.

58 J. Lin, M.-H. Lee, Z.-P. Liu, C. Chen and C. J. Pickard, Mechanism for linear and nonlinear optical effects in β-BaB_2O_4 crystals, *Phys. Rev. B: Condens. Matter Mater. Phys.*, 1999, **60**, 13380–13389.

59 K. Liu, J. Han, F. Li, C. Jin, Z. Yang, M. Mutailipu and S. Pan, $Ba_2B_{13}O_{19}(OH)_5{\cdot}5H_2O$: A promising nonlinear optical material with a unique $^2[B_{13}O_{19}(OH)_5]_\infty$ two-dimensional layer, *J. Alloys Compd.*, 2022, **897**, 163194.

60 P. Gong, L. Kang and Z. Lin, Realizing deep-ultraviolet second harmonic generation by first-principles-guided materials exploration in hydroxyborates, *J. Am. Chem. Soc.*, 2020, **142**, 15157–15163.

61 J.-H. Huang, C.-C. Jin, P.-L. Xu, P. Gong, Z. Lin, J.-W. Cheng and G.-Y. Yang, $Li_2CsB_7O_{10}(OH)_4$: A deep-ultraviolet nonlinear-optical mixed-alkaline borate constructed by unusual heptaborate anions, *Inorg. Chem.*, 2019, **58**, 1755–1758.

62 Y. Wang, S. Pan, X. Tian, Z. Zhou, G. Liu, J. Wang and D. Jia, Synthesis, structure, and properties of the noncentrosymmetric hydrated borate $Na_2B_5O_8(OH){\cdot}2H_2O$, *Inorg. Chem.*, 2009, **48**, 7800–7804.

63 Q. Liu, X. Zhang, Z. Yang, F. Zhang, L. Liu, J. Han, Z. Li and S. Pan, $K_3B_3O_4(OH)_4{\cdot}2H_2O$: A UV nonlinear optical crystal with isolated $[B_3O_4(OH)_4]^{3-}$ anion groups, *Inorg. Chem.*, 2016, **55**, 8744–8749.

64 R. S. Poulin and J. D. Grice, Volkovskite, a complex borate mineral: Refined crystallographic data and optics, *Can. Mineral.*, 2013, **51**, 157–169.

65 R. K. Rastsvetaeva, V. I. Andrianov, E. A. Genkina, T. N. Sokolova and A. A. Kashaev, Crystal structure of volkovskite $KCa_4B_{22}O_{32}(OH)_{10}Cl{\cdot}4H_2O$ from Nepkii deposit (E. Siberia), *Kristallografiya*, 1992, **37**, 326–333.

66 D. J. MacDonald and F. C. Hawthorne, The crystal chemistry of Si-Al substitution in tourmaline, *Can. Mineral.*, 1995, **33**, 849–858.

67 S. A. Vinogradova, D. Y. Pushcharovsky, A. V. Arakcheeva and O. V. Dimitrova, Crystal structure of new decaborate $Na_2Ba_2[B_{10}O_{17}(OH)_2]$, *Crystallogr. Rep.*, 2002, **47**, 24–28.

68 Z.-H. Liu, L.-Q. Li and M.-Z. Wang, Synthesis, crystal structure and thermal behavior of $Na_4[B_{10}O_{16}(OH)_2]{\cdot}4H_2O$, *J. Alloys Compd.*, 2006, **407**, 334–339.

69 E. Corazza, S. Menchetti and C. Sabelli, The crystal structure of nasinite, $Na_2[B_5O_8(OH)]{\cdot}2H_2O$, *Acta Crystallogr., Sect. B: Struct. Crystallogr. Cryst. Chem.*, 1975, **31**, 2405–2410.

70 Q.-M. Qiu, X.-Y. Li, C.-A. Chen, K.-N. Sun and G.-Y. Yang, Polar polymorphism: β-$Ca_2[B_5O_8(OH)]_2[B(OH)_3]{\cdot}H_2O$-synthesis, structure and nonlinear optical property, *J. Solid State Chem.*, 2021, **299**, 122193.

71 L. Wang, S. Pan, L. Chang, J. Hu and H. Yu, UV nonlinear optical crystal $Ba_2[B_6O_9(OH)_4]$ featuring unique chiral layers with a new $B_{18}O_{42}$ circle based on BO_3 and BO_4 units, *Inorg. Chem.*, 2012, **51**, 1852–1858.

72 P. Becker, P. Held and L. Bohatý, Crystal growth and optical properties of the polar hydrated pentaborates Rb$[B_5O_6(OH)_4]{\cdot}2H_2O$ and $NH_4[B_5O_6(OH)_4]{\cdot}2H_2O$ and structure redetermination of the ammonium compound, *Cryst. Res. Technol.*, 2000, **35**, 1251–1262.

73 N. A. Yamnova, S. M. Aksenov, S. Y. Stefanovich, A. S. Volkov and O. V. Dimitrova, Synthesis, crystal structure refinement, and nonlinear-optical properties of $CaB_3O_5(OH)$: Comparative crystal chemistry of calcium triborates, *Crystallogr. Rep.*, 2015, **60**, 649–655.

74 B.-H. Lei, Z. Yang and S. Pan, Enhancing optical anisotropy of crystals by optimizing bonding electron distribution in anionic groups, *Chem. Commun.*, 2017, **53**, 2818–2821.

